Available online at www.sciencedirect.com
ScienceDirect
Trans. Nonferrous Met. Soc. China 33(2023) 107−127
Transactions of Nonferrous Metals Society of China
www.tnmsc.cn

Microstructure evolution, deformation behavior and manufacture design of TiAl matrix composites reinforced with in-situ borides precipitation

Ming-ao LI[1,2,3], Juan LI[1], Tao ZHOU[1], Li HU[1], Lai-xin SHI[1], Yu-yong CHEN[2,3], Li-juan XU[3], Shu-long XIAO[2,3]

1. School of Materials Science and Engineering, Chongqing University of Technology, Chongqing 400054, China;
2. National Key Laboratory of Science and Technology on Precision Heat Processing of Metals, Harbin Institute of Technology, Harbin 150001, China;
3. School of Materials Science and Engineering, Harbin Institute of Technology, Harbin 150001, China

Received 26 September 2021; accepted 29 March 2022

Abstract: Phase transformation and borides precipitation caused by boron addition influence microstructure evolution and deformation behavior of in-situ TiAl matrix composites. Dynamic recrystallization mechanism and dynamic recovery mechanism were investigated by isothermal compression tests, scanning electron microscopy and transmission electron microscopy, etc. The value of apparent deformation activation energy (Q) of present composites is calculated to be 691.506 kJ/mol. In the temperature range of 1100−1200 °C, nucleation and growth of recrystallized γ and α grains promoted by TiB obstacles dominate the deformation below or above $T_{\alpha_2\rightarrow\alpha}$. The dynamic recovery of α phase dominates the deformation in condition with low strain rates at 1250 °C. Boron addition increases the fraction of α phase and decreases the transformation temperatures of $\gamma\rightarrow\alpha$ and $\alpha_2\rightarrow\alpha$, which promotes the nucleation and growth of recovered α grains during the loading. Deformation mechanisms and processing performance were also clarified based on the reestablished constitutive model.

Key words: in-situ TiAl matrix composite; boride; deformation mechanism; microstructure evolution; dynamic recrystallization (DRX); dynamic recovery (DRV)

1 Introduction

TiAl matrix composites are promising lightweight structural materials for elevated-temperature applications in the aerospace and weapons industries, due to high specific strength, excellent creep resistance, corrosion resistance and oxidation resistance [1−3]. Several in-situ synthesis ceramic reinforcements have been added to improve mechanical properties of TiAl composites, such as TiB, Ti_5Si_3, Ti_2AlN and Ti_2AlC, etc [4−7]. LI et al [6] reported that TiB precipitation enhanced dramatically ultimate tensile strength (UTS) of high niobium containing TiAl alloys from 510 to 657 MPa at 850 °C. The authors thought that the stripe-shaped TiB could cause dislocation pile-ups to strengthen TiAl based alloys at high temperatures.

Different types of borides precipitation and grain refinement induced by boron addition can contribute to excellent mechanical properties of TiAl matrix composites [8,9]. TiB with structure of $B27$ and B_f are primarily found in TiAl matrix composites, and the common structure of borides is mainly presented as orthorhombic $B27$-TiB [10]. Primary $B27$-TiB always maintains orientation relationship $(001)[010]_{TiB}//(0001)\langle 1120\rangle_{\alpha_2}$ with α_2 phase, while the secondary $B27$-TiB usually exhibits the orientation relationship $(11\bar{2})[1\bar{1}0]_{\gamma}//(100)[0\bar{1}0]_{TiB}$ with γ phase [11,12]. LIU et al [12] found that $B27$-TiB particles were highly enriched

Corresponding author: Ming-ao LI, E-mail: limingao@cqut.edu.cn; Shu-long XIAO, E-mail: xiaoshulong@hit.edu.cn
DOI: 10.1016/S1003-6326(22)66094-1

with Nb element, but Nb element destabilized B_f-TiB. The size and the morphology of borides in variant TiAl matrix composites are closely related to alloying element species and solidification conditions, which distinctly lead to borides formation [13]. KARTAVYKH et al [9] found that prevailing *B*27-TiB occurred in high niobium containing TiAl alloys, and thin plates or flakes were parallel to the ribbon plane in this type of TiB precipitation.

HU [14] has proven that large-sized borides were detrimental to plastic deformation and reduced ductility. LI et al [15] reported that TiB occurrence would promote dynamic recrystallization of high niobium containing TiAl alloys. With the boron content increasing, the critical strain of dynamic recrystallization decreased from $0.826\varepsilon_p$ to $0.67\varepsilon_p$, which meant the much earlier activation of dynamic recrystallization. Above recent studies partly indicated that the effect of boron addition on deformation behavior was probably related to dislocation movement, phase transformation and borides precipitation, etc. However, the detailed microstructure evolution and deformation mechanisms of TiAl matrix composite with borides precipitation have not been reported. Meanwhile, forging or rolling is thought as the important manufacturing method for TiAl matrix composite in aerospace industry. Thus, it is necessary to clarify deformation mechanisms and processing performance of in-situ TiAl matrix composites with borides precipitation, which is important for manufacture design and further application of the materials.

In this work, the main objectives are to investigate microstructure evolution, dynamic recrystallization mechanism and dynamic recovery mechanism of in-situ TiAl matrix composite with borides precipitation during the isothermal compression by scanning electron microscopy (SEM), electron back-scattered diffraction (EBSD) and transmission electron microscopy (TEM).

2 Experimental

In-situ TiAl matrix composites containing borides precipitation with a composition of Ti−43Al−6Nb−1Mo−1Cr−0.6B (at.%) were produced by induction skull melting (ISM) and melted under an Ar atmosphere (pressure of ~800 Pa). The present materials contained Ti bar (99.99 wt.%), pure Al (99.99 wt.%), pure Cr (99.99 wt.%), Al−Nb alloys (52.4 at.% Nb), Al−Mo (50.5 at.% Mo) alloys and TiB_2 powders (99.99 wt.%). The electromagnetic stirring was conducted for 300 s in melting condition to ensure raw materials mixing uniformly. The melting temperature was above 1600 °C, and the holding time was 6−7 min at about 1560 °C during the melting to promote the adequate reaction of different components. Finally, the as-cast ingots with mass of about 800 g and size of *d*50 mm × 100 mm were obtained. The as-cast ingots were then hot isostatic pressed (HIPed) at 1200 °C for 4 h under a pressure of 140 MPa and aged at 900 °C for 48 h. The main purposes of hot isostatic pressing treatment were to eliminate the casting defects (e.g. shrinkage porosity, shrinkage cavity and porosity) and the effect of casting defects on the further deformation, meanwhile, not to change the cast microstructure obviously.

The specimens (*d*8 mm × 12 mm) were used in isothermal compression tests which were carried out in Gleeble 1500D instrument. Deformation temperatures were 1100, 1150, 1200 and 1250 °C; strain rates were 0.001, 0.01, 0.1 and 1.0 s^{-1}; heating rate was 10 °C/s; engineering strain was 50% (≈0.69 true strain). The microstructures were observed by scanning electron microscopy (SEM), electron back-scattered diffraction (EBSD) and transmission electron microscopy (TEM). The EBSD test was carried out in scanning electron microscope HELIOS NanoLab 600i with an accelerating voltage of 20 kV and step size of 0.5 μm. The data were analyzed via OIM 6.1 software. Grain boundaries with misorientation angle of 2°−5°, 5°−15° and >15° were determined as low angle rain boundary (LAGB), medium angle grain boundary (MAGB) and high angle grain boundary (HAGB), respectively. The scanned phases were measured as $D0_{19}$-α_2, $L1_0$-γ and *B*2-β, respectively.

3 Results and discussion

3.1 Initial cast/HIPed microstructure

The initial cast/HIPed microstructures of in-situ TiAl matrix composites with borides precipitation are shown in Fig. 1. The (α_2+γ) lamellar colonies exhibit as equiaxed crystal, and the stripe-shaped borides (e.g marked by arrow)

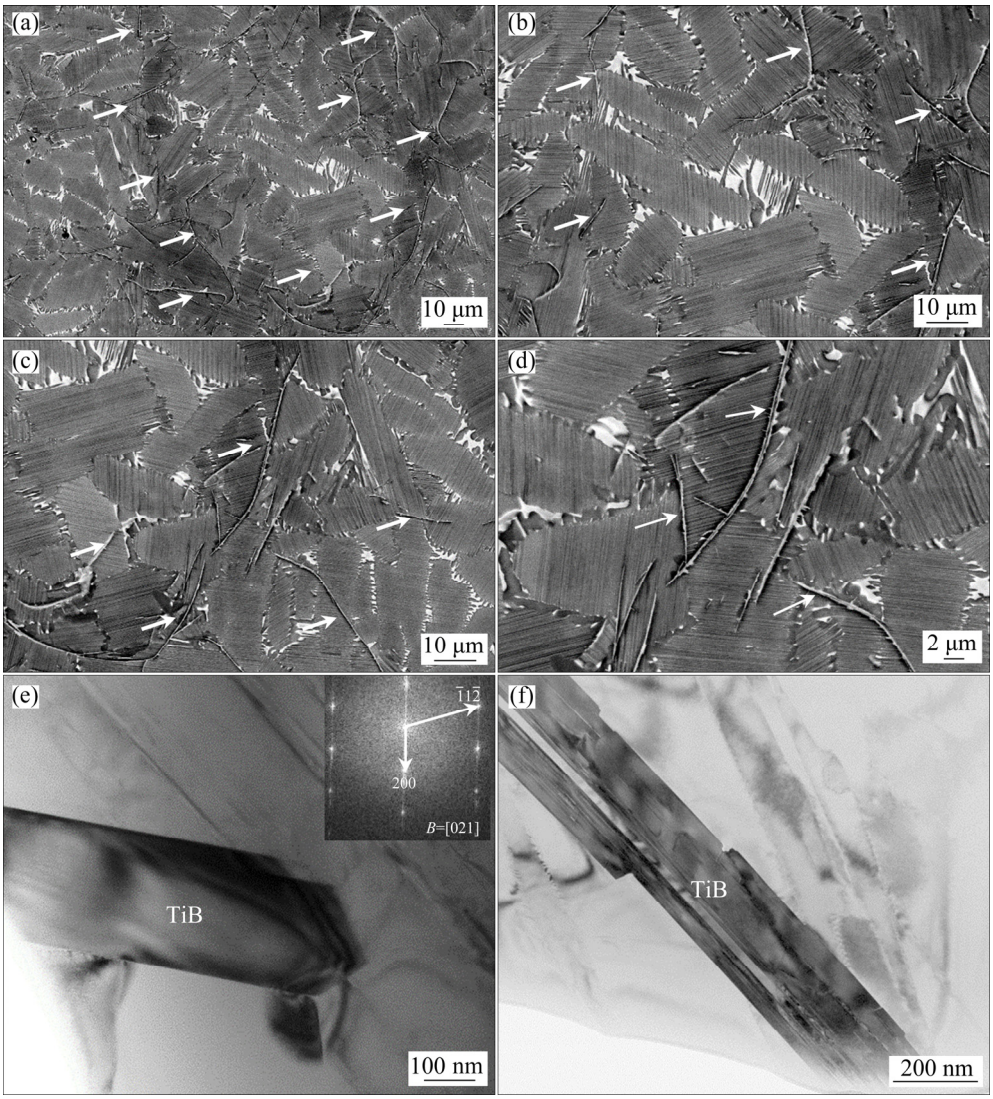

Fig. 1 Initial cast/HIPed microstructure: (a−d) SEM images with various magnification; (e, f) TEM image and SAED pattern with [021] axis

precipitate, as exhibited in Figs. 1(a−d). When nucleation takes place in borides from β at higher temperature, α grains nucleation on borides surfaces or many possible α grains result in grain refinement of TiAl based alloys [10]. Compared to TiAl alloys without boron addition [16], it can be found that the sizes of (α_2+γ) lamellar colonies decrease, columnar crystals transform to equiaxed crystal, the segregation disappear and stripe-shaped borides appear along the boundaries of (α_2+γ) lamellar colonies in the initial cast/HIPed microstructures of composites with boron addition. The stripe-shaped borides are indicated as TiB by the selected area electron diffraction (SAED) pattern in Figs. 1(e, f). GRAEF et al [17] thought that borides always appeared as TiB in TiAl based alloys, when the content of Al element did not exceed 44 at.%. KARTAVYKH et al [9] and LIU et al [12] reported that borides exhibited mostly as *B*27 structure in high niobium containing TiAl alloys, due to *B*27-TiB stabilizing niobium. Above references support the conclusion that stripe-shaped borides are TiB in the initial cast/HIPed microstructure of present composites. The phase transformation, the (α_2+γ) lamellar colonies and the TiB obstacles can influence deformation behavior of TiAl composites [15].

3.2 Microstructure evolution during deformation

The deformed microstructures of in-situ TiAl matrix composites with borides precipitation in various conditions are exhibited in Figs. 2 and 3. As shown in Figs. 2(a−c, e−g), a large number of

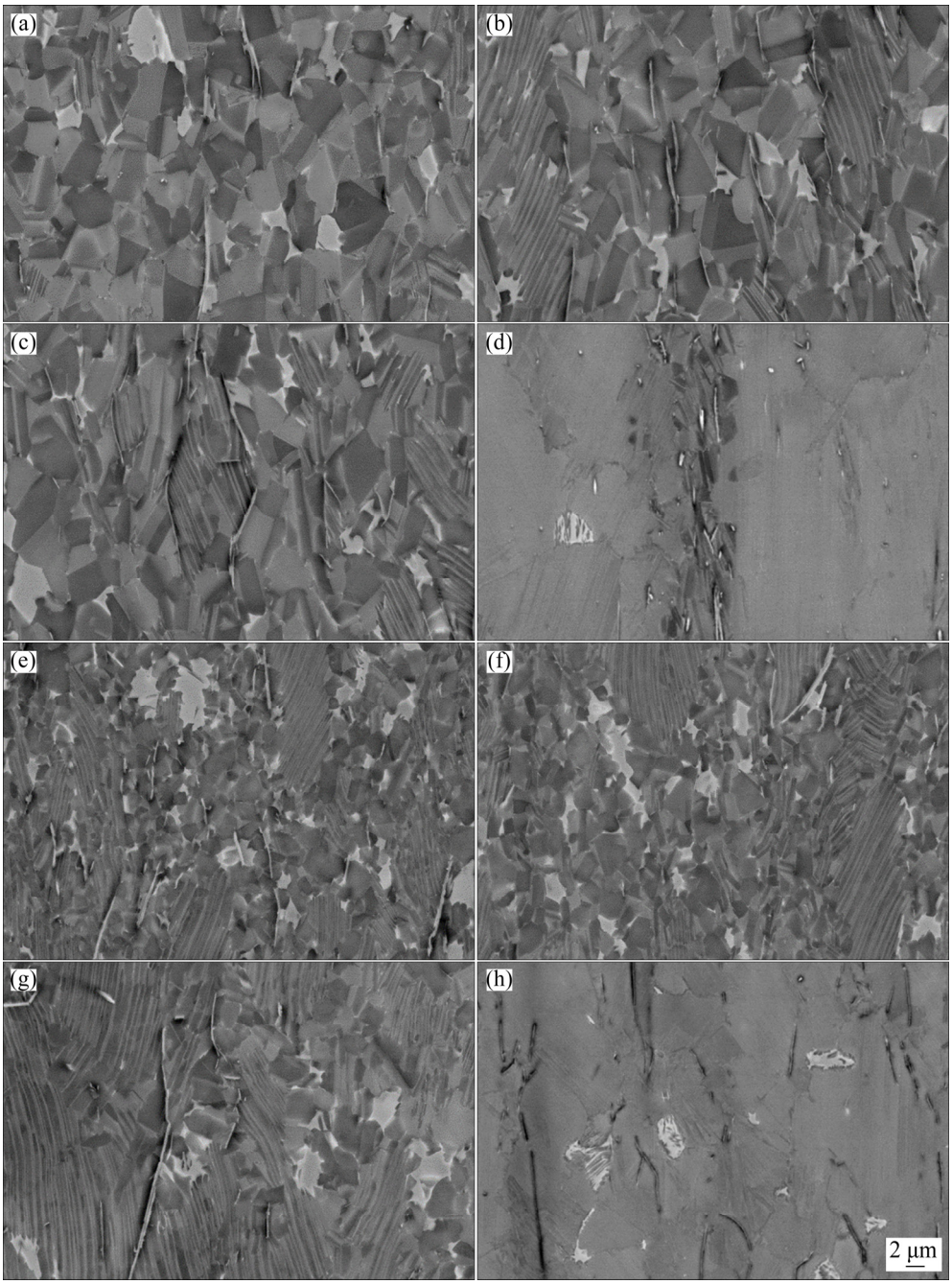

Fig. 2 Deformed microstructures at different temperatures and strain rates of 0.001 s^{-1} and 0.01 s^{-1}: (a) 1100 °C, 0.001 s^{-1}; (b) 1150 °C, 0.001 s^{-1}; (c) 1200 °C, 0.001 s^{-1}; (d) 1250 °C, 0.001 s^{-1}; (e) 1100 °C, 0.01 s^{-1}; (f) 1150 °C, 0.01 s^{-1}; (g) 1200 °C, 0.01 s^{-1}; (h) 1250 °C, 0.01 s^{-1}

recrystallized grains nucleate in condition with low strain rates (0.001−0.01 s^{-1}) below 1200 °C. The recrystallized grains always appear around the TiB obstacles or colony boundaries in the composites. In Figs. 2(a−c, e−g), the recrystallized grains nucleation on the both sides or/and on the one of the sides of TiB obstacles can be observed. The nucleation of recrystallized grains depends on the fault stacking energy, which is mainly related to dislocations and twinning.

LI et al [18] thought that borides were generally considered as heterogeneous nucleation and boundaries pinning sites during deformation. The authors reported that the dynamic recrystallization in Ti−43Al−4Nb−1.4W−0.6B alloys was controlled by the rates of interfaces formation, due to low migration rates. With the strain increasing, meanwhile, broken borides led to increased fraction of interfaces, and then broken borides acted as nucleation sites to promote

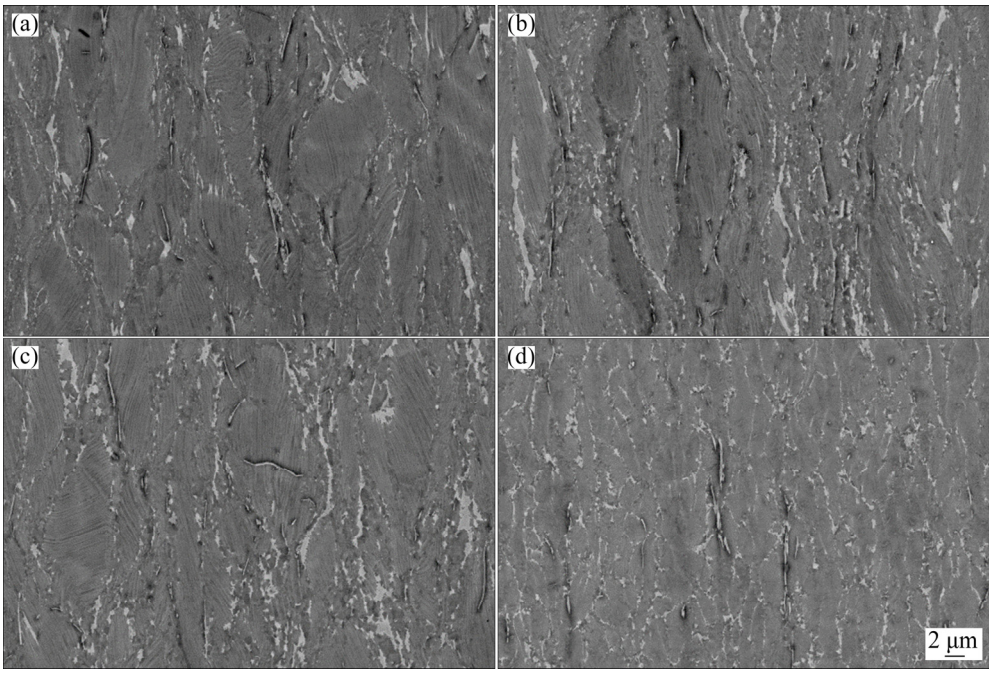

Fig. 3 Deformed microstructures at different temperatures and strain rate of 0.1 s^{-1}: (a) 1100 °C; (b) 1150 °C; (c) 1200 °C; (d) 1250 °C

recrystallized grains nucleation. SCHWAIGHOFER et al [19] indicated that the occurrence of β phase, silicide and H-type carbides could promote dynamic recrystallization and refine grains in TNM (Ti−43Al−4Nb−1Mo−0.1B (at.%)) alloys. LI et al [15] thought that dislocation pile-ups caused by TiB obstacles could promote recrystallized grains nucleation, and the increased fraction of (α_2+γ) lamellar colony boundaries caused by boron addition could provide much more positions for recrystallized grains nucleation. In combination with above researches, the reason of dynamic recrystallization promoted by borides in the present composite is generally related to dislocation pile-ups and twinning, etc. In Figs. 2(d, h), it can be observed that (α_2+γ) lamellar colonies and little recrystallized grains with small size occur in condition with low strain rates (0.001−0.01 s^{-1}), with the temperature further increasing to 1250 °C. Additionally, recrystallized grains hardly nucleate with the strain rate exceeding 0.1 s^{-1}, as exhibited in Fig. 3. The deformation of α_2/γ lamellae perpendicular to compression direction indicates an unstable deformation.

3.2.1 Deformed microstructure under various conditions

(1) Effect of deformation temperature on microstructure evolution

The deformed microstructure of in-situ TiAl matrix composites in condition of 1100 °C, 0.001 s^{-1} is shown in Fig. 4. The orientation and distribution of grains are exhibited clearly in Figs. 4(a, b), by which different grains in the deformed microstructure can be distinguished. As shown in Fig. 4(c), it can be seen that the fractions of γ, α_2 and β phase are 63.1%, 22.1% and 11.9%, respectively. Expect for (α_2+γ) lamellar colonies, the fraction of recrystallized γ grains exceeds 50.0%, while the fractions of recrystallized α_2 and β grains are less than 22.1% and 11.9%, respectively. In Fig. 4(d), the fraction of grain boundaries with large angle occupies more than 92.5%, which indicates a large number of recrystallized grains nucleation. It has been reported that the dominant (89±3)°⟨100] misorientation angle within recrystallized γ phase, γ-phase 60°⟨111⟩ pseudo and 70°⟨110⟩ true twin boundaries operated the dynamic recrystallization of γ phase [20,21]. Thus, parts of grain boundaries with large angles appear within recrystallized grains, as shown in Fig. 4(d).

The deformed microstructure of in-situ TiAl matrix composites in condition of 1150 °C, 0.001 s^{-1} is shown in Fig. 5. Compared to grains distribution maps in Figs. 4(a, b), it can be found that the average size and the fraction of recrystallized grains are enhanced in Figs. 5(a, b),

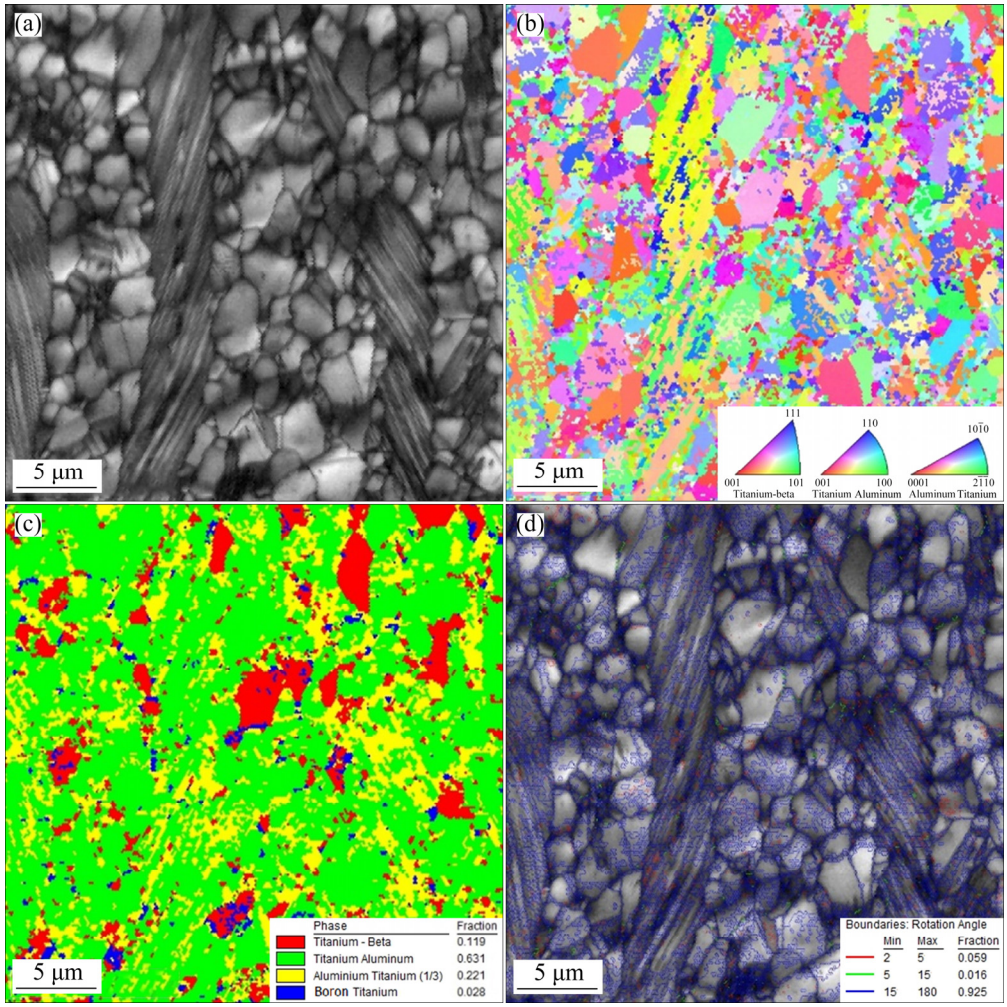

Fig. 4 Deformed microstructures in condition of 1100 °C, 0.001 s^{-1}: (a) SEM image; (b) Grains distribution; (c) Phase distribution; (d) Distribution of boundaries angle

with the temperature increasing. In Fig. 5(c), the fractions of recrystallized γ, α_2 and β grains are 39.1%, 48.1% and 9.2%, respectively. The high fraction of grain boundaries with large rotation angle in Fig. 5(d) indicates the occurrence of complete dynamic recrystallization in this condition. Meanwhile, the deformed microstructure of in-situ TiAl matrix composites in condition of 1200 °C, 0.001 s^{-1} can be observed in Fig. 6. The fractions of recrystallized γ, α_2 and β grains are indicated as 39.3%, 48.8% and 12.9%, respectively, as shown in Fig. 6(c). The high fraction of grain boundaries with large rotation angle in Fig. 6(d) also indicates the occurrence of complete dynamic recrystallization in this condition.

(2) Effect of strain rate on microstructure evolution

The deformed microstructure of in-situ TiAl matrix composites in condition of 1200 °C, 0.01 s^{-1} is shown in Fig. 7. It can be seen that the fractions of recrystallized γ, α_2 and β grains are 57.0%, 33.6% and 7.4%, respectively, in Fig. 7(c), with the strain rate increasing from 0.001 to 0.01 s^{-1}. The high fraction of grain boundaries with large angle in Fig. 7(d) indicates the complete dynamic recrystallization in this condition. The higher strain rates provide insufficient time for nucleation and growth of recrystallized grains, which leads to decreased average sizes of recrystallized grains. Expect for the large misorientation angle, the twinning interfaces and the grain boundaries with misorientation >15° are also the reasons for the large-angle grain boundaries within the recrystallized γ and α grains, as shown in Figs. 4(d), 5(d), 6(d) and 7(d).

In order to clarify the relationship between TiB, recrystallized grains nucleation and dislocation, the bright-field TEM images of in-situ TiAl matrix

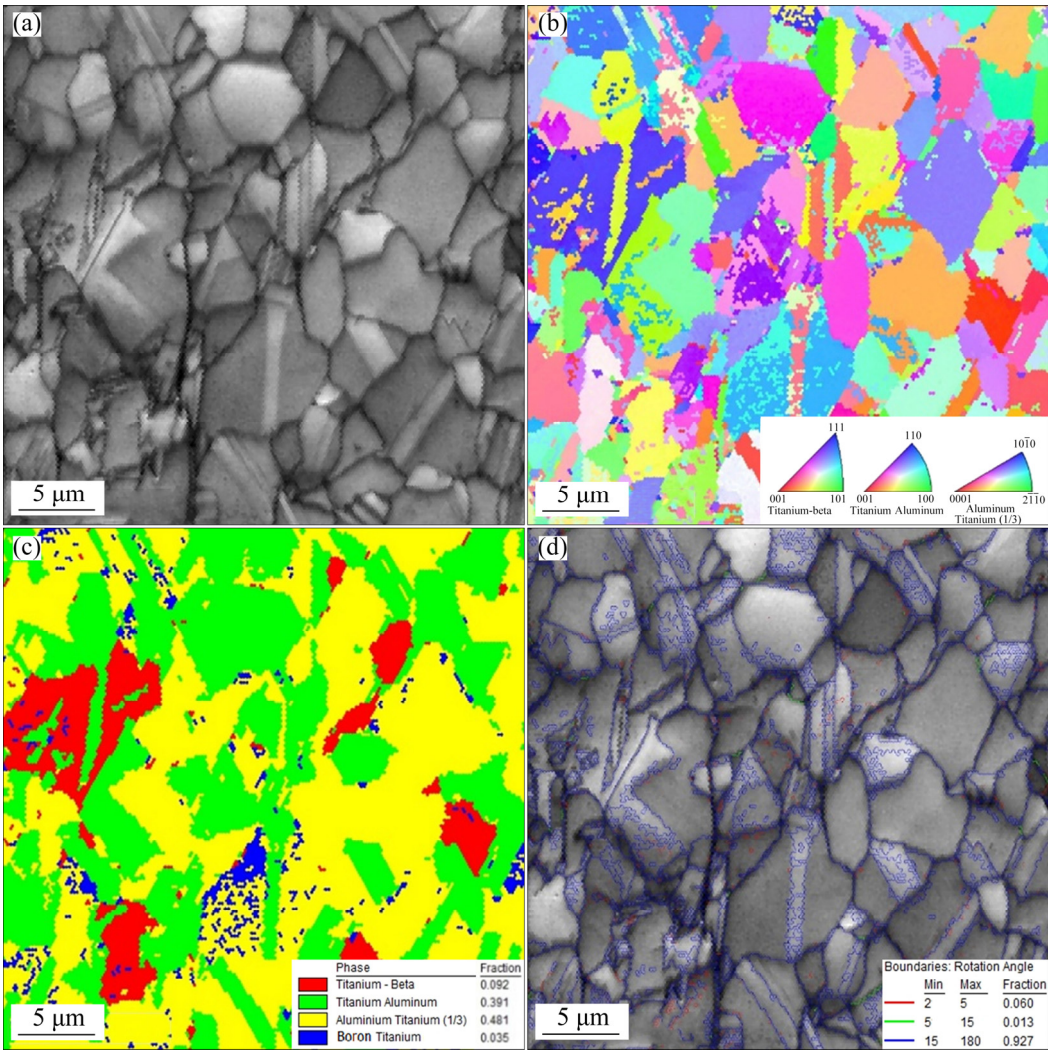

Fig. 5 Deformed microstructures in condition of 1150 °C, 0.001 s^{-1}: (a) SEM image; (b) Grains distribution; (c) Phase distribution; (d) Distribution of boundaries angle

composites in different conditions are displayed in Fig. 8. In Fig. 8(a), it can be observed that TiB obstacles pin dislocation slipping and lead to dislocation pile-ups in condition 1100 °C, 0.001 s^{-1}. As exhibited in Fig. 8(b), recrystallized grains nucleation and dislocation pile-ups appear around the broken TiB. Meanwhile, the nucleation of recrystallized grains on the interfaces of TiB obstacles can also be seen in Fig. 8(c). The similar microstructure observation also happened in recent research, as shown in Fig. 8(d) [15]. In combination with recent researches about the relationship between the reinforcement and the recrystallized grains [15,18,19], it is indicated that TiB can cause dislocation pile-ups to promote the nucleation of recrystallized grains during the loading. Additionally, YE et al [22] thought that Ti_2AlC inclusions served as an effective obstacle to cause dislocation pile-ups and induced recrystallization nucleation. Moreover, the recrystallized grain growth was significantly restricted, due to an obstructive effect of Ti_2AlC particles on grain boundary migration. The authors indicated that the reinforcement could induce the nucleation of recrystallized grains, and meanwhile, it also restrained the growth of recrystallized grains, due to the dispersion at grain boundaries. Thus, TiB obstacles lead to the refinement of recrystallized grains in present TiAl composites, compared to alloys without boron addition [23].

Summarily, as shown in Figs. 4−7, the fraction of recrystallized α_2 grains increases, the fraction of recrystallized γ grains decreases, and the fraction of recrystallized β grains almost maintains stable, with

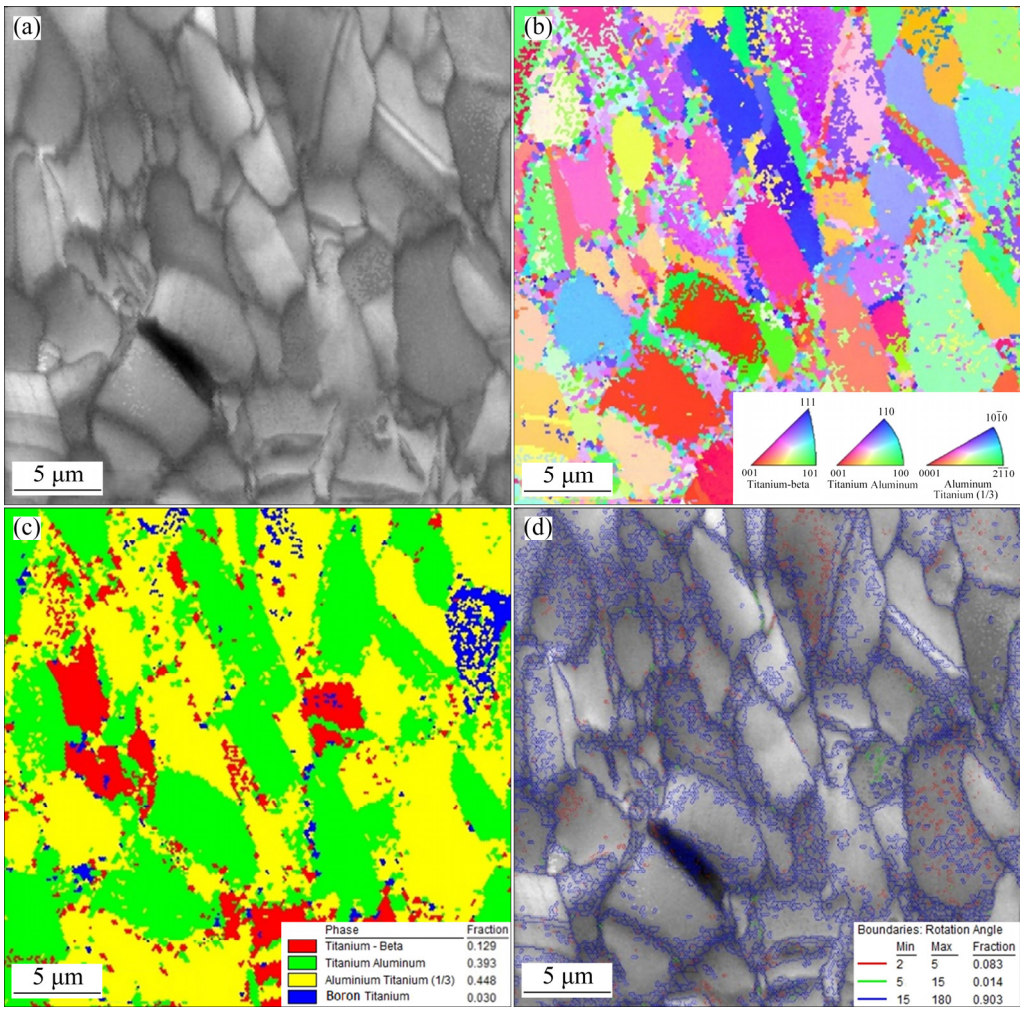

Fig. 6 Deformed microstructures in condition of 1200 °C, 0.001 s^{-1}: (a) SEM image; (b) Grains distribution; (c) Phase distribution; (d) Distribution of boundaries angle

the temperature increasing below 1200 °C. The content of α phase increases under $\gamma \rightarrow \alpha$ phase transformation, and the structure of α phase transforms from ordered $D0_{19}$ to disordered $A3$, with the temperature increasing [24−26]. $L1_0$-γ phase is softer than $D0_{19}$-α_2 phase, while $A3$-α phase is softer than $L1_0$-γ phase [25]. Thus, $D0_{19}$-α_2 and γ phase mainly provide deformation resistance below and above $\alpha \rightarrow \alpha_2$ transformation temperature ($T_{\alpha \rightarrow \alpha_2}$), respectively. This causes the dynamic recrystallization within γ phase and $A3$-α phase below and above $T_{\alpha \rightarrow \alpha_2}$, respectively. Additionally, boron can expand α phase region, promote α phase formation and decrease $T_{\alpha \rightarrow \alpha_2}$ [12]. All of these dramatically lead to increased fraction of recrystallized α_2 grains and decreased fraction of recrystallized γ grains with the temperature increasing. With the temperature further increasing to 1200 °C, disordered $A3$-α and $A2$-β phase lead to dynamic recovery in condition with low strain rates (0.001−0.01 s^{-1}), as shown in Figs. 2(d, h). LI et al [23] investigated microstructure evolution and deformation mechanism of high niobium containing TiAl alloys. They found that nucleation and growth of recrystallized γ and α grains dominated the deformation below or above $T_{\alpha_2 \rightarrow \alpha}$, respectively, in the temperature range of 1100−1200 °C. Thus, the dynamic recrystallization mechanisms of in-situ TiAl matrix composites with borides can be analyzed as follows, in combination with the recent study [23].

3.2.2 Dynamic recrystallization mechanisms

(1) Dynamic recrystallization mechanism in temperature range from 1100 °C to $T_{\alpha \rightarrow \alpha_2}$

In the temperature range from 1100 °C to $T_{\alpha \rightarrow \alpha_2}$, slipping systems in the β phase with $A2$

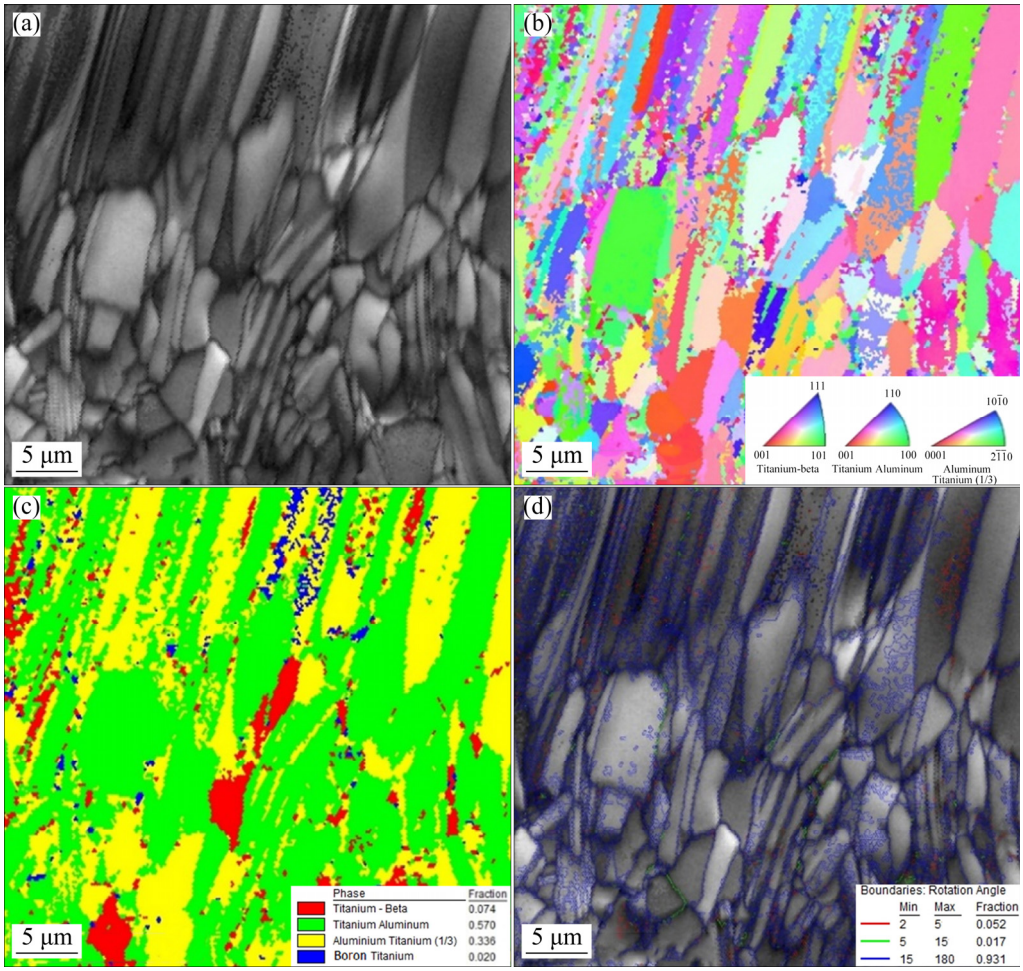

Fig. 7 Deformed microstructures in condition of 1200 °C, 0.01 s^{-1}: (a) SEM image of recrystallized grains; (b) Grains distribution; (c) Phase distribution; (d) Distribution of boundaries angle

structure are easy to be activated during the loading. The α phase with high fault energy presents ordered $D0_{19}$ structure. The γ phase presents ordered $L1_0$ structure with four teams of slipping systems and four teams of twinning systems on the {111} crystal plane. TiB obstacles can hinder lamellae deformation and dislocation gliding to promote dynamic recrystallization. Summarily, the quantity sequence of activated slipping systems is β>γ>α>TiB [27,28]. As shown in Fig. 9(a), β, γ, α phases and TiB distribute in this ideal order, in which the activated slipping system is arranged from the most to the lest during loading. Additionally, it is indicated that the fraction of β phase in present materials is less than 10% [29−31]. The fraction of α phase is enhanced and stays in the range of 30%−40%, due to boron addition. The fraction of γ phase exceeds 50% in the thermodynamic equilibrium. In this case, therefore, the fraction of γ phase is much larger than that of β and α phases in the thermodynamic equilibrium.

As shown in Fig. 9(a), dislocations pile up in the front of β/γ interfaces during the loading and promote the nucleation of recrystallized β grains firstly. Due to the low resistance of activated slipping systems along 1/2⟨110]{111} within γ phase, most dislocations traverse easily through β phase into γ phase and do not pile up the in front of the β/γ interface. In combination with the low fraction of β/β_0 phase (<10%), less recrystallized β grains nucleate, due to insufficient fault energy and dislocation pile-ups. Additionally, in the cell of α phase with $D0_{19}$ structure, the deformation resistance along the c axis is large, and the coordination deformation along different directions seems to be hard. The large deformation resistance of α phase hinders dislocation gliding during the loading, and then dislocations pile up within the

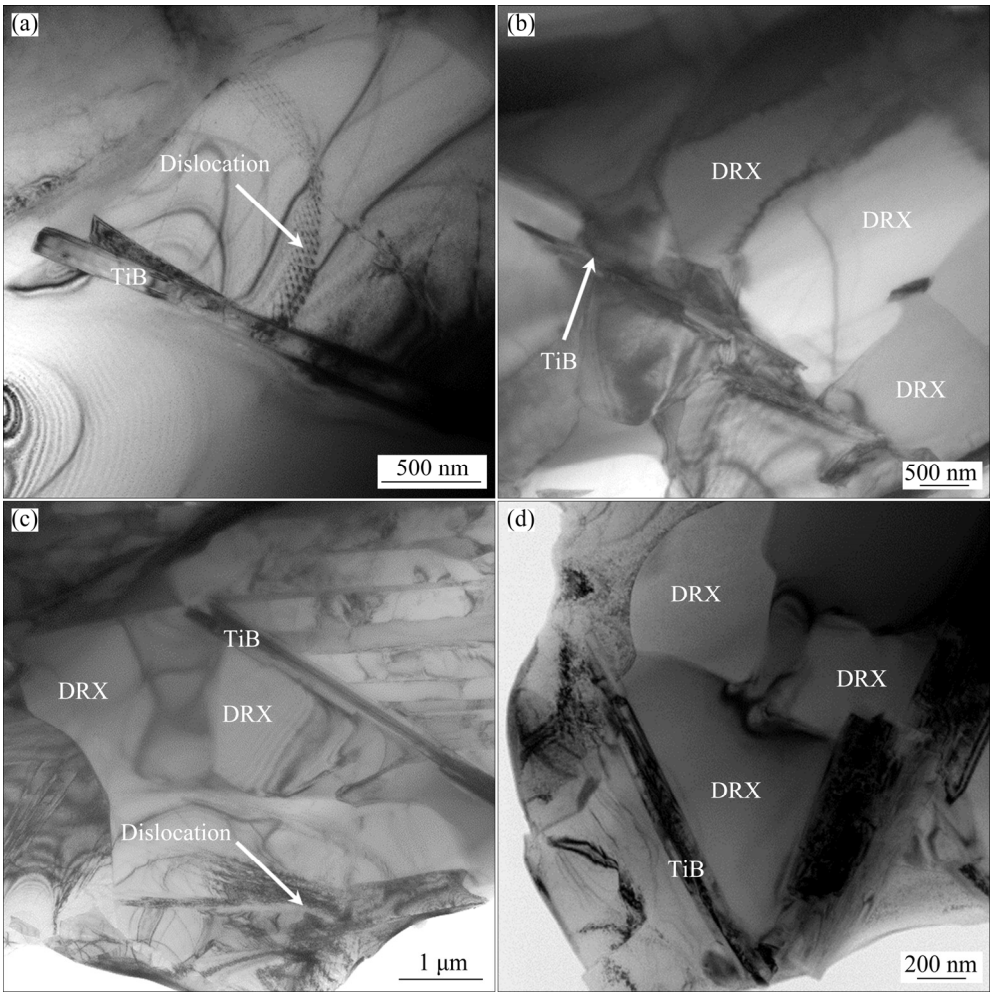

Fig. 8 TEM images of TiB, dislocation pile-ups and recrystallized grains within deformed microstructures in different condition: (a) 1100 °C, 0.001 s^{-1}; (b, c) 1150 °C, 0.001 s^{-1}; (d) 1200 °C, 0.001 s^{-1} [15]

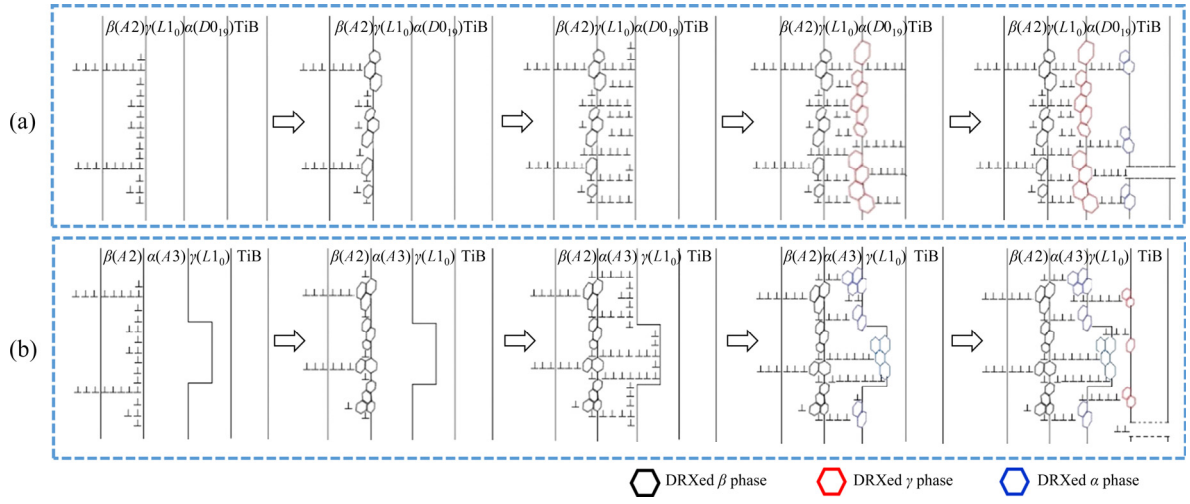

Fig. 9 Dynamic recrystallization mechanism in different temperature ranges: (a) From 1100 °C to $T_{\alpha\rightarrow\alpha_2}$; (b) From $T_{\alpha\rightarrow\alpha_2}$ to 1200 °C

γ phase in the front of the γ/α interface. This promotes the nucleation of a large number of recrystallized γ grains in the front of the γ/α interface, due to high fraction of γ phase (>50%) in this case. Afterwards, parts of dislocations slip into α phase and cause the nucleation of recrystallized α

grains. Due to TiB obstacles and increased fraction of α phase caused by boron addition, the nucleation of recrystallized α_2 phase is promoted, and the fraction of recrystallized α grains is enhanced.

Except this ideal type of phase distribution, dislocation pile-ups in the front of β/γ, β/α and β/β interfaces with low fraction cause the nucleation of less recrystallized β grains. A large number of dislocation pile-ups in the front of γ/α and γ/γ interfaces with high fraction can promote the nucleation of much more recrystallized γ grains. Additionally, the fraction of α phase is increased by boron addition, and TiB obstacles promote the nucleation and growth of recrystallized grains. Thus, compared to the materials without boron addition [23], the fraction of recrystallized α_2 grains is enhanced, but it is still lower than the fraction of recrystallized γ grains in this case. As exhibited in Fig. 9(a), this type of dynamic recrystallization mechanism conforms to the results in Fig. 4 exactly, in which the volume fraction of recrystallized γ grains is larger than that of recrystallized β and α_2 grains.

(2) Dynamic recrystallization mechanism in temperature range from $T_{\alpha\rightarrow\alpha_2}$ to 1200 °C

In the temperature range from $T_{\alpha\rightarrow\alpha_2}$ to 1200 °C, α phase transforms from ordered $D0_{19}$ structure to disordered $A3$ structure, which leads to another type of dynamic recrystallization mechanism in present composites. As shown in Fig. 9(b), β, γ, α phases and TiB distribute in the order (β>α>γ>TiB) that activated slipping systems arrange from the most to the lest during the loading. With the temperature increasing, additionally, the fraction of β phase maintains stable, the fraction of α phase increases, and the fraction of γ phase decreases dramatically [29−31]. Meanwhile, the fraction of α phase is enhanced dramatically by boron addition. Thus, the fraction of recrystallized β phase is the lowest in the present composites, due to the low fraction of β phase (<10%) and the insufficient resistance for dislocations. The α/γ and α/TiB interfaces with dramatically increased fraction lead to the nucleation of abundant recrystallized α_2 grains in this temperature range. The fraction of recrystallized γ grains is also promoted by TiB obstacles and dislocation pile-ups. However, the fraction of recrystallized γ grains is less than that of recrystallized α_2 grains, due to the decreased fraction of γ phase in this case. Summarily, the fraction of recrystallized α_2 grains is larger than that of recrystallized β and γ grains, as shown in Figs. 5 and 6.

3.2.3 Dynamic recovery mechanism at 1250 °C

As shown in Figs. 2(d, h), recrystallized γ and α grains hardly nucleate but only equiaxed (α_2+γ) lamellar colonies appear within the deformed microstructure in conditions of 1250 °C, 0.01 s^{-1} and 1250 °C, 0.001 s^{-1}. LI et al [23] reported that the deformation mechanism of Ti−43Al−6Nb−1Mo−1Cr alloys mainly depended on dynamic recovery caused by sub-grains, grain boundary bulging, dislocation gliding and vacancies diffusion at 1250 °C. QIANG et al [32] found that the dynamic recovery of single α phase in TiAl based alloys was dominated by the characteristic stages, i.e., the grain boundary bulging with the formation of symmetrical-tilt boundaries near boundary bulging regions, and the sub-grain formation at bulged boundary regions by evolving symmetrical-tilt boundaries into asymmetrical-tilt or tilt−twist boundaries.

With the temperature increasing to 1250 °C, the fraction of γ phase further decreases and nearly approaches to 0%, and the fraction of α phase dramatically increases to nearly 90% [29−31]. The fraction of β/β_0 phase is still less than 10%, while β phase presents a disordered structure in this condition. Thus, the dynamic recovery of disordered α phase dominates the deformation of the present composites. The slipping systems on the cylinder $\{1\bar{1}00\}\langle11\bar{2}0\rangle$ and inter area $(0001)\langle11\bar{2}0\rangle$ of the α cell become easy to be activated during the loading. When dislocations slip into grain boundaries and move out of the grains, the atomic steps form and cause boundaries bulging. And then, dislocations are multiplicated and start to accumulate in the front of grain boundaries. Afterwards, the low-angle grain boundaries evolve into high angle through the progressive accumulation of dislocations. Due to boron addition, the fraction of α phase is enhanced and the grains are refined. The fraction of colony boundaries with high-density dislocations is increased, which can promote sub-grains formation, grain boundary bulging and dislocation gliding. Meanwhile, the stress concentration in the front of the grain boundaries leads to TiB breaking. Finally,

the equiaxed α phase transforms to γ and α_2 lamellae, and the (α_2+γ) lamellar colonies are formed during the water-cooling after deformation. Meanwhile, β phase transforms to β_0 phase and broken TiB occurs in the deformed microstructure with dynamic recovery, as shown in Figs. 2(d, h).

3.3 Deformation behavior

3.3.1 Flow stress curves

To explain deformation mechanisms and predict manufacture performance, the flow stress curves of in-situ TiAl matrix composites with borides precipitation in various conditions are shown in Fig. 10. It can be observed that flow stress curves display a stress peak during the initial deformation, due to the work hardening. Dynamic recrystallization always appears before the peak stress. After the peaks, dynamic recrystallization and dynamic recovery lead to flow stress decreasing firstly rapidly and then slowly, with the strain increasing. In the temperature range of 1150−1200 °C, the obvious stress peaks indicate the activated dynamic recrystallization after work hardening. Additionally, with the temperature further increasing to 1250 °C, the flow stress curves correspond to the microstructure evolution with dynamic recovery well in condition with low strain rates (0.001−0.01 s^{-1}). No obvious stress peaks appear in conditions of 1250 °C, 0.001 s^{-1} and 1250 °C, 0.01 s^{-1}. During the dynamic recovery, the flow stress curves maintain stability, due to sub-grain formation, grain boundary bulging and dislocation gliding within disordered α phase. Especially, the flow stress curve in condition 1250 °C, 0.001 s^{-1} displays a slightly increasing tendency during the dynamic recovery. Due to the activated slipping systems within various matrix phases, TiB is insufficient to hinder dislocation gliding but can cause parts of stress concentration. With dislocation piling-up, TiB breaking and dislocation further slipping, the stress concentration likely leads to the flow stress curve increasing slightly in this condition.

3.3.2 Constitutive model reestablishment and analysis

The relationship of metallic materials between deformation temperature, strain rate and flow stress by Arrhenius is exhibited as Eqs. (1)−(3) [33].

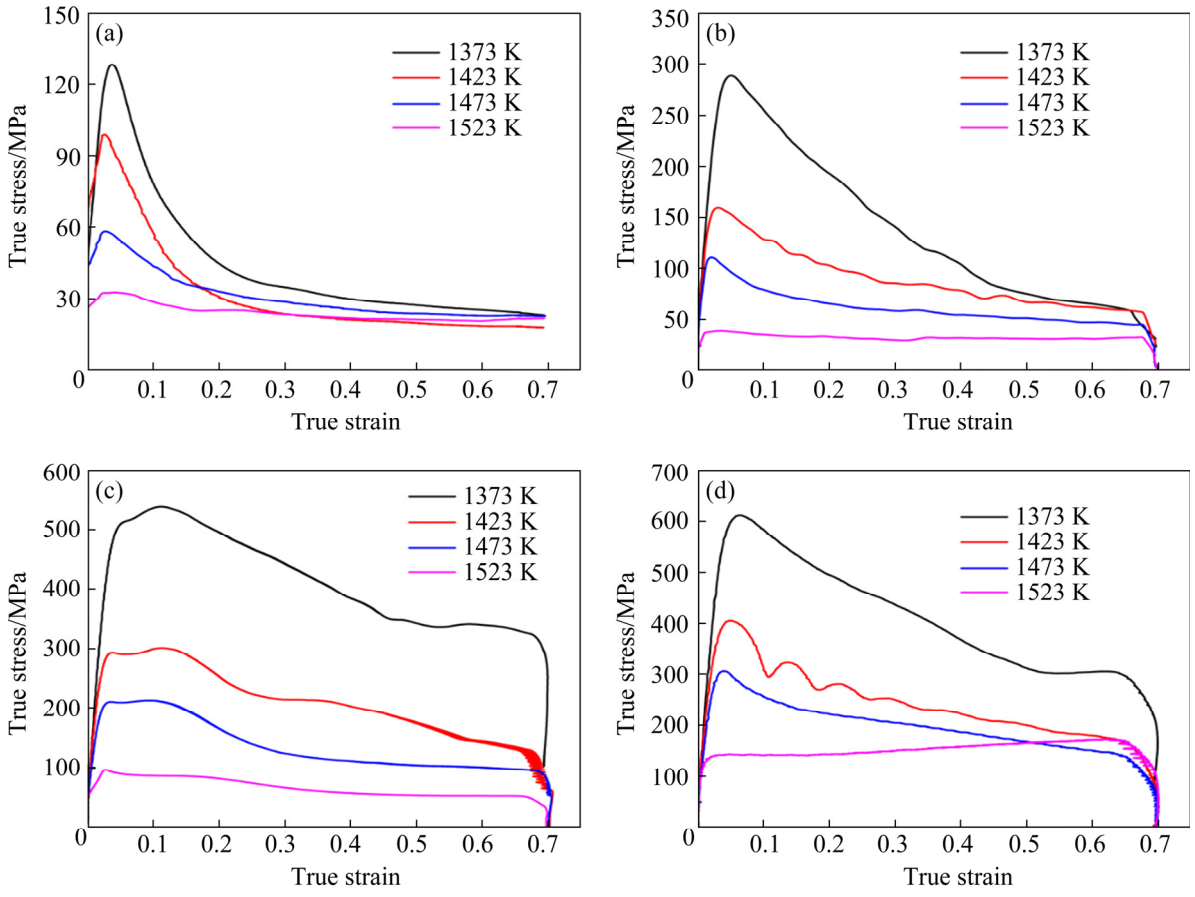

Fig. 10 Flow stress curves at different strain rates and temperatures: (a) 0.001 s^{-1}; (b) 0.01 s^{-1}; (c) 0.1 s^{-1}; (d) 1.0 s^{-1}

Boron addition causes TiB precipitation, grain refinement and variety of phase transformation, which influences flow stress curves, dynamic recrystallization and dynamic recovery. Thus, the constitutive model of present composites is reestablished for exact prediction of deformation behavior:

$$\dot{\varepsilon}=A[\sinh(\alpha\sigma)]^{n}\exp[-Q/(RT)] \quad (1)$$

$$\dot{\varepsilon}=A_1(\alpha\sigma)^{n_1}\exp[-Q/(RT)] \quad (\alpha\sigma<0.8) \quad (2)$$

$$\dot{\varepsilon}=A_2\exp(\beta\sigma)\exp[-Q/(RT)] \quad (\alpha\sigma>1.2) \quad (3)$$

where R is molar gas constant (8.3145 J/(mol·K)), $\dot{\varepsilon}$ is strain rate (s^{-1}), σ is flow stress (MPa), Q represents deformation activation energy (kJ/mol), T represents deformation temperature (K), n represents stress exponent, and A, A_1, A_2, α ($\alpha=\beta/n_1$) and β are material constants. The material constants β, n_1, n and n_3 can be calculated by the fitting line slopes of $\ln\dot{\varepsilon}-\sigma$, $\ln\dot{\varepsilon}-\ln\sigma$, $\ln\dot{\varepsilon}-\ln[\sinh(\sigma\alpha)]$ and $\ln[\sinh(\sigma\alpha)]-T^{-1}$ curves, as exhibited in Fig. 11. As shown in Eq. (4), deformation apparent activation energy (Q) of in-situ TiAl matrix composites is calculated to be 695.51 kJ/mol. Compared to TiAl based alloys [34,35], deformation activation energy of present composites displays a higher value. The higher Q value indicates a harder achievement of dynamic recrystallization, dislocation movement and plastic deformation in the same condition. In combination with microstructure analysis, TiB obstacles hinder dislocation gliding and lamellae deformation, which increases the difficulty for deformation activation. This presumably leads to an increased deformation activation energy for in-situ TiAl matrix composites with TiB precipitation.

$$Q=R\left[\frac{\partial\ln\dot{\varepsilon}}{\partial\ln[\sinh(\alpha\sigma)]}\right]_T\left[\frac{\partial\ln[\sinh(\alpha\sigma)]}{\partial(1/T)}\right]_{\dot{\varepsilon}}=Rnn_3 \quad (4)$$

In order to illustrate the dependence of flow stress (σ) on temperature (T) and strain rate ($\dot{\varepsilon}$), the Zener−Hollomon parameter (Z) is exhibited as Eq. (5). The calculated hyperbolic sine relationship between Z and peak flow stress is displayed by fitting line in Fig. 12. The intercept ($\ln A$) can be obtained and A can be calculated as 3.8×10^{23}, and then the constitutive equation of the composites can

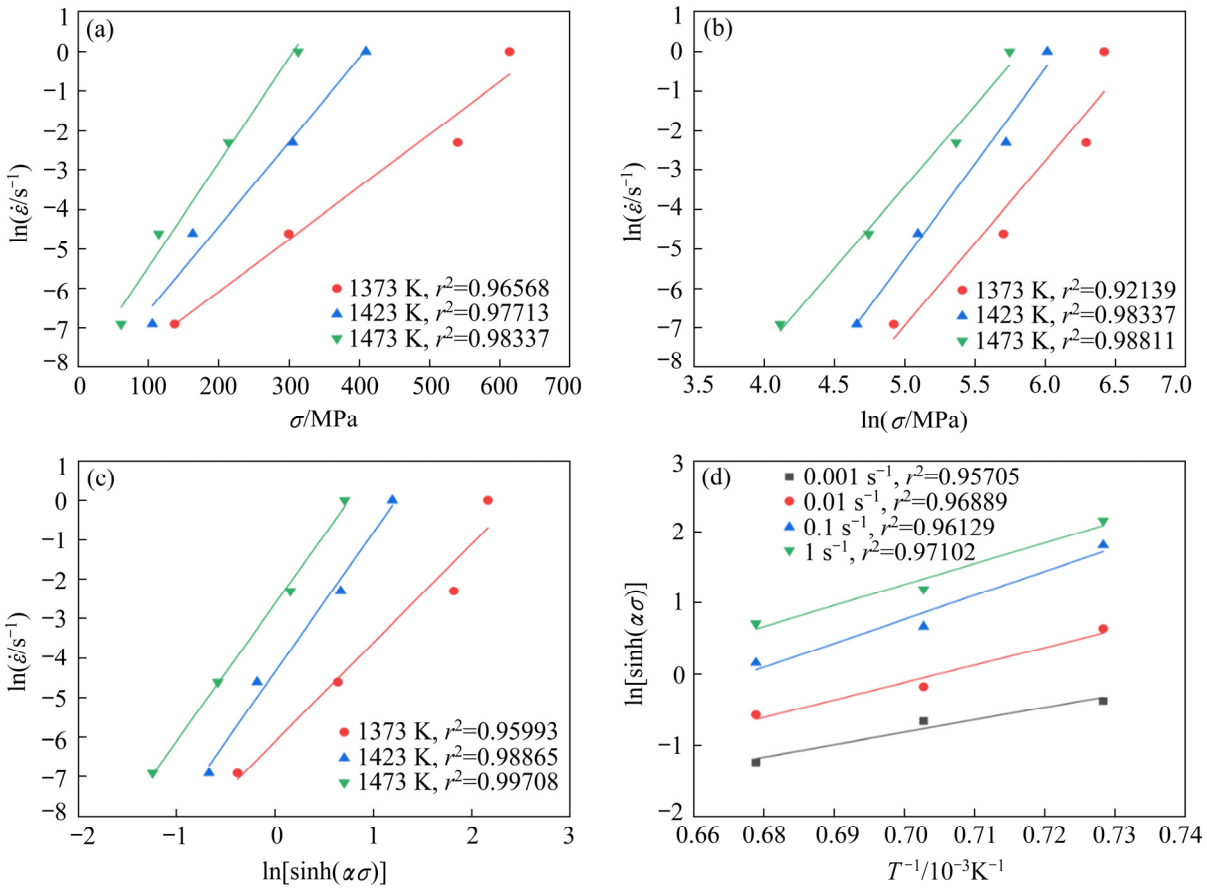

Fig. 11 Linearly fitting relationship of $\ln\dot{\varepsilon}-\sigma$ (a), $\ln\dot{\varepsilon}-\ln\sigma$ (b), $\ln\dot{\varepsilon}-\ln[\sinh(\alpha\sigma)]$ (c), and $\ln[\sinh(\alpha\sigma)]-T^{-1}$ (d)

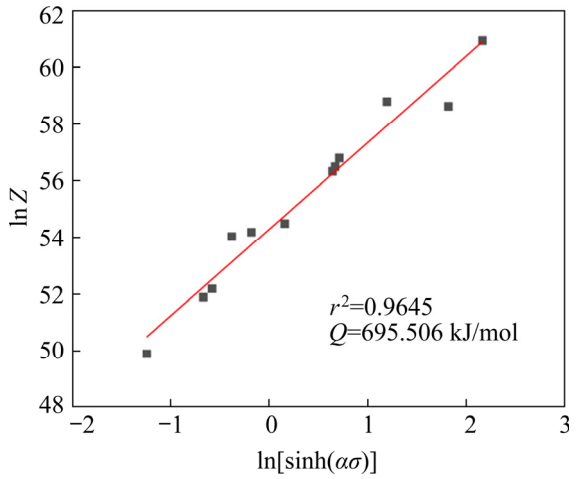

Fig. 12 Relationship between ln Z and ln[sinh($\alpha\sigma$)]

be established as Eq. (6):

$$Z=\dot{\varepsilon}\exp\left(\frac{Q}{RT}\right)=A[\sinh(\alpha\sigma)]^n \quad (5)$$

$$\dot{\varepsilon}=3.8\times10^{23}[\sinh(0.00466\sigma)]^{3.05}\exp(-\frac{695506}{8.314T}) \quad (6)$$

LIN et al [36] and WANG et al [37] reported that plastic strain could influence material constants significantly within the entire strain range. For the accurate prediction of flow stress variety, the material constants in various strains are calculated, as listed in Table 1. The obvious differences can be seen with the variety of the strain. Thus, it is necessary to take the strain effect into account. Based on the principle of regression analysis, the relationship between material constants and strain is depicted by polynomial fitting. As given in Table 2, the sixth order polynomial is applied to calculating the theoretical flow stress of the composites. Meanwhile, the regression curves of material constants and the theoretical flow stress curves are exhibited in Figs. 13 and 14.

3.3.3 Processing map analysis

Based on the flow stress curves, hot processing maps of in-situ TiAl matrix composites with borides precipitation with different strains are calculated to obtain suitable processing parameters. The processing map always consists of power dissipation map and instability regime map. The dynamic materials model (DMM) of metallic materials illustrates that input power is usually applied to two components from outer system, as shown in Eq. (7) [38]:

Table 1 Calculated material constants (α, Q, n and ln A) of present TiAl matrix composites

ε	α	Q/(J·mol^{-1})	n	ln A
0.025	0.0070	759640	3.2068	58.4347
0.05	0.0071	833850	2.7373	64.4342
0.075	0.0079	806850	2.5239	62.1368
0.1	0.0084	764110	2.3814	58.6556
0.125	0.0090	730950	2.2420	55.8975
0.15	0.0093	684550	2.1544	52.1399
0.175	0.0099	674420	2.1568	51.3280
0.2	0.0101	647750	2.1523	49.1914
0.225	0.0103	632660	2.1456	47.9960
0.25	0.0105	605160	2.1372	45.8097
0.275	0.0105	580520	2.1236	43.8660
0.3	0.0107	570780	2.1154	43.0987
0.325	0.0107	548590	2.1258	41.3245
0.35	0.0107	517890	2.1376	38.8341
0.375	0.0109	500020	2.1112	37.3884
0.4	0.0110	471680	2.1191	35.0863
0.425	0.0112	453370	2.1195	33.6096
0.45	0.0114	420650	2.1110	30.9188
0.475	0.0116	417490	2.1064	30.6631
0.5	0.0117	398340	2.1232	29.1129
0.525	0.0120	390290	2.1255	28.4496
0.55	0.0122	388100	2.1220	28.2603
0.575	0.0123	391260	2.1259	28.5350
0.6	0.0126	388310	2.1123	28.2714
0.625	0.0127	387920	2.1236	28.2416
0.65	0.0130	387660	2.1698	28.2170
0.675	0.0149	439650	2.3258	32.3956
0.7	0.0201	633950	2.8653	48.3104

$$P=\sigma\dot{\varepsilon}=G+J=\int_0^{\dot{\varepsilon}}\sigma\mathrm{d}\varepsilon+\int_0^{\dot{\varepsilon}}\varepsilon\mathrm{d}\sigma \quad (7)$$

where P is instantaneous dissipated power, G represents energy dissipation by plastic work, and J is energy dissipation through microstructure changes.

The relationship between flow stress σ and strain rate stress $\dot{\varepsilon}$ at a certain temperature can be depicted as Eq. (8), where m represents flow stress sensitivity, and K is material constant. Flow stress sensitivity (m) represents the relationship between flow stress and strain rate. The efficiency of power

Table 2 Relationship between material constants and ε by sixth degree polynomial

Constant	Equation
α	$0.00813-0.06679\varepsilon+1.24816\varepsilon^2-7.44549\varepsilon^3+20.50185\varepsilon^4-26.58597\varepsilon^5+13.14245\varepsilon^6$
Q	$765.46576+1378.59217\varepsilon-18545.38012\varepsilon^2+55089.72726\varepsilon^3-48794.64618\varepsilon^4-39201.0699299999\varepsilon^5+62591.83375\varepsilon^6$
n	$3.90489-34.0954\varepsilon+279.13262\varepsilon^2-1199.21833\varepsilon^3+2783.02489\varepsilon^4-3279.45044\varepsilon^5+1532.53701\varepsilon^6$
$\ln A$	$59.0513+106.65708\varepsilon-1483.35246\varepsilon^2+4479.61684\varepsilon^3-4128.10777\varepsilon^4-2908.98448\varepsilon^5+4947.8273\varepsilon^6$

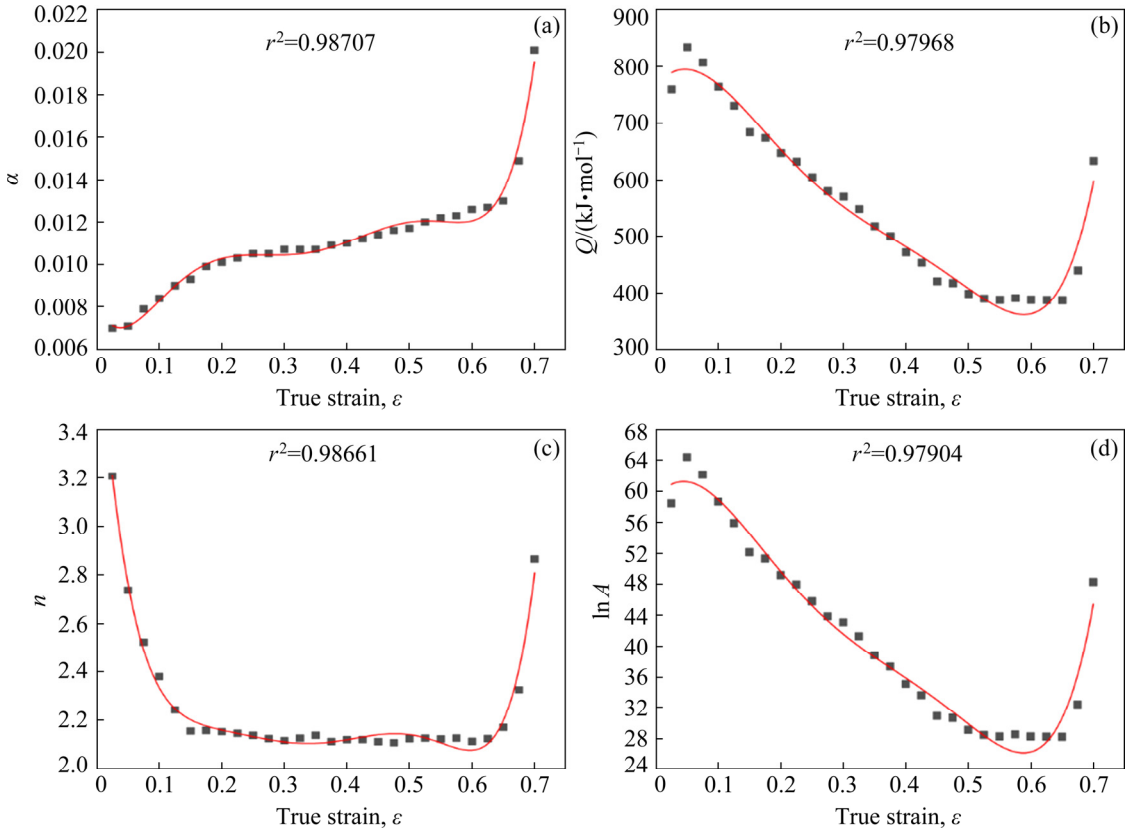

Fig. 13 Polynomial fitting results of material constants: (a) ε–α; (b) ε–Q; (c) ε–n; (d) ε–ln A

dissipation (η) represents the rate of micro-structure evolution, compared with an ideal linear dissipater [39,40]. When the material is supposed as an ideal linear dissipation body (m=1), J obtains the maximum, as given in Eq. (9):

$$\sigma=K\dot{\varepsilon}^m \tag{8}$$

$$J_{\max}=1/2\sigma\dot{\varepsilon} \tag{9}$$

According to the Murty criterion widely applied to various $\sigma-\dot{\varepsilon}$ curves, G is expressed as Eq. (10), in which $\dot{\varepsilon}_{\min}$ represents the minimum strain rate. The power dissipation (η) defined as $J/J_{\max}$ is a dimensionless parameter, as given in Eq. (11). On account of maximum principles of irreversible thermodynamics, an instability criterion (Murty instability criterion) [41,42] is used to predict sprout of flow instability ($2m<\eta$). The unstable flow caused by adiabatic shear occurs, when all powers are converted into viscoplastic heat (J=0), which means $\eta\leq 0$. Thus, only when the domains locate in the ranges of $0<\eta<2m$ and $0<m<1$, materials will deform stably with a sufficient dynamic recrystallization.

$$G=\int_0^{\dot{\varepsilon}}\sigma\mathrm{d}\dot{\varepsilon}=\int_0^{\dot{\varepsilon}_{\min}}\sigma\mathrm{d}\dot{\varepsilon}+\int_{\dot{\varepsilon}_{\min}}^{\dot{\varepsilon}}\sigma\mathrm{d}\dot{\varepsilon}=\left(\frac{\sigma\dot{\varepsilon}}{m+1}\right)_{\dot{\varepsilon}=\dot{\varepsilon}_{\min}}+\int_{\dot{\varepsilon}_{\min}}^{\dot{\varepsilon}}\sigma\mathrm{d}\dot{\varepsilon} \tag{10}$$

$$\eta=\frac{J}{J_{\max}}=\frac{P-G}{J_{\max}}=2\left(1-\frac{1}{\sigma\dot{\varepsilon}}\int_0^{\dot{\varepsilon}}\sigma\mathrm{d}\dot{\varepsilon}\right)=2\left[1-\left(\left[\frac{\sigma\dot{\varepsilon}}{m+1}\right]_{\dot{\varepsilon}=\dot{\varepsilon}_{\min}}+\int_{\dot{\varepsilon}_{\min}}^{\dot{\varepsilon}}\sigma\mathrm{d}\dot{\varepsilon}\right)\Big/\sigma\dot{\varepsilon}\right] \tag{11}$$

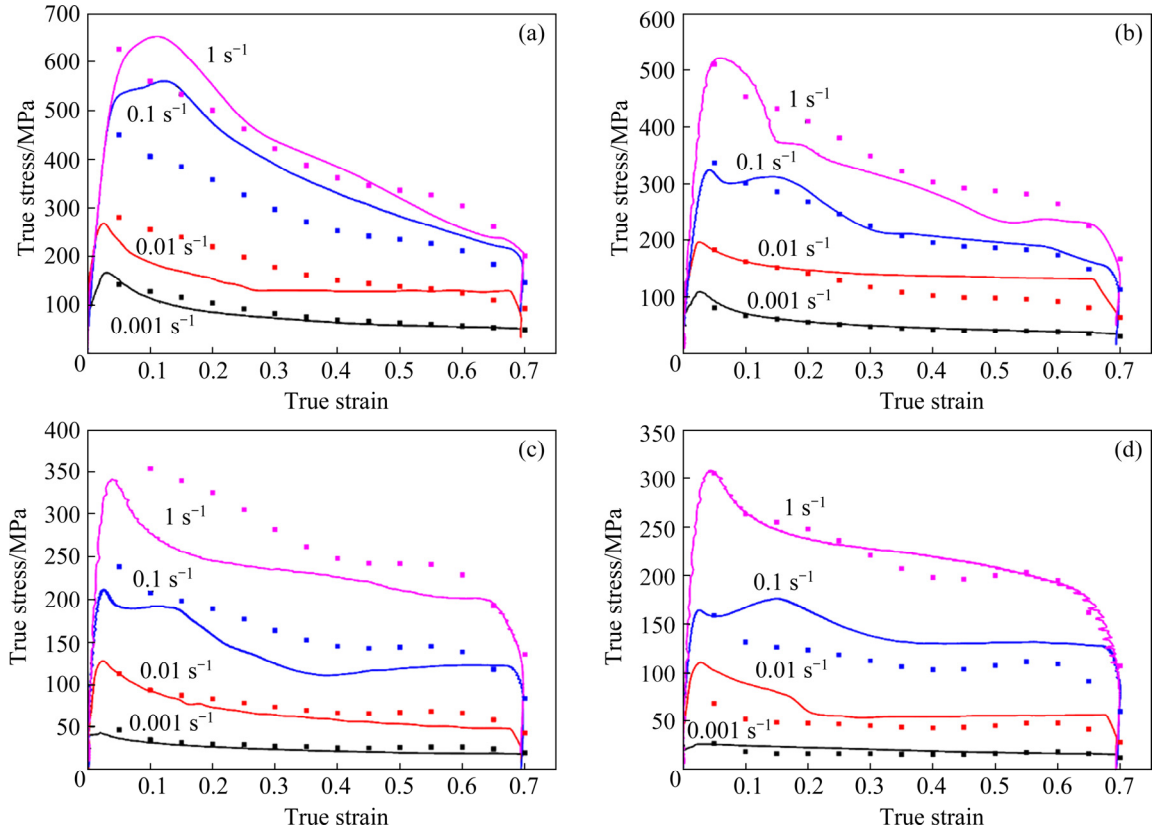

Fig. 14 Measured and calculated flow stress curves at different temperatures and strain rates: (a) 1100 °C; (b) 1150 °C; (c) 1200 °C; (d) 1250 °C

The power dissipation maps of in-situ TiAl matrix composites with borides precipitation by Murty instability criterion are calculated (Fig. 15). As shown in Figs. 15(a−e), the kinked contour lines in condition with low strain rates (<0.1 s^{-1}) and a temperature range of 1100−1200 °C indicate the appearance of dynamic recrystallization. In these conditions, the most energy is applied to nucleation and growth of recrystallized γ and α_2 grains, which conforms to the deformation mechanisms in temperature range of 1100−1120 °C. PRASAD and SESHACHARYULU [43] thought that dynamic recrystallization usually occurs in the η range of 0.4−0.5. In Fig. 15, the rational values of power dissipation for microstructure evolution are 0.57, 0.55, 0.52, 0.51, 0.52 and 0.53, with the strain increasing from 0.2 to 0.7. The recrystallized γ and α_2 grains nucleate in the stable processing region with low strain rates and in a temperature range of 1100−1120 °C. The peak power dissipation usually stays in the left bottom of the power dissipation maps, which conforms to the deformed microstructure in conditions of 1150 °C, 0.01 s^{-1}; 1150 °C, 0.001 s^{-1} and 1200 °C, 0.01 s^{-1}.

The hot processing maps of in-situ TiAl matrix composites with borides precipitation by Murty instability criterion are exhibited in Fig. 16. The shadow regions in the hot processing maps represent unstable plastic deformation, in which the $\xi(\dot{\varepsilon})$ is less than 0 and the local deformation or adiabatic shear band appears. The unstable regions always occur in the upper left corner of processing maps with lower temperatures and higher strain rates, while the shear cracks with 45° appear within the samples. The upper right corner of processing maps with higher temperatures and higher strain rates also represents another unstable region, in which samples crack seriously. In Fig. 3, the deformed microstructure in condition of (1100−1250 °C), 0.1 s^{-1} corresponds to the processed alloys in unstable region. The hot processing maps with the maximum strain in Fig. 16(f) display the extreme deformation stage, in which the unstable region expands dramatically. Summarily, cracks and adiabatic shear band usually appear in the region with high strain rates (≥0.1 s^{-1}) and low temperatures (<1150 °C), while flow instability

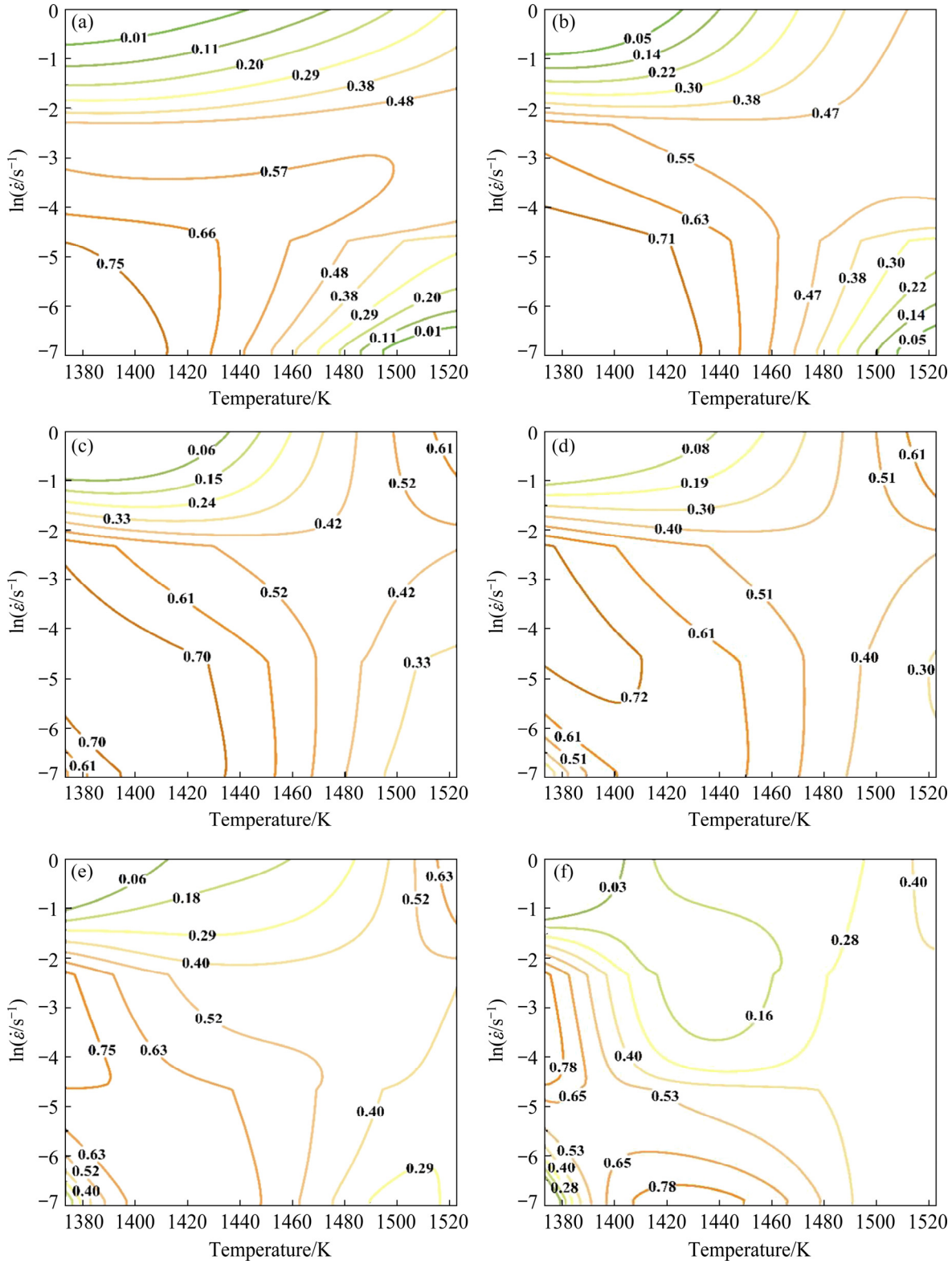

Fig. 15 Power dissipation maps by Murty instability criterion with various strains: (a) ε=0.2; (b) ε=0.3; (c) ε=0.4; (d) ε=0.5; (e) ε=0.6, (f) ε=0.7

occurs in the region with high strain rates (≥0.1 s^{-1}) and higher temperatures (1150−1200 °C). Dynamic recrystallization of γ and α phases usually happens below or above $T_{\alpha\rightarrow\alpha_2}$ in condition with lower strain rates (<0.1 s^{-1}) and a temperature range of 1100−1200 °C. Dynamic recovery of α phase starts in condition with lower strain rates (0.001−0.01 s^{-1}) above 1250 °C.

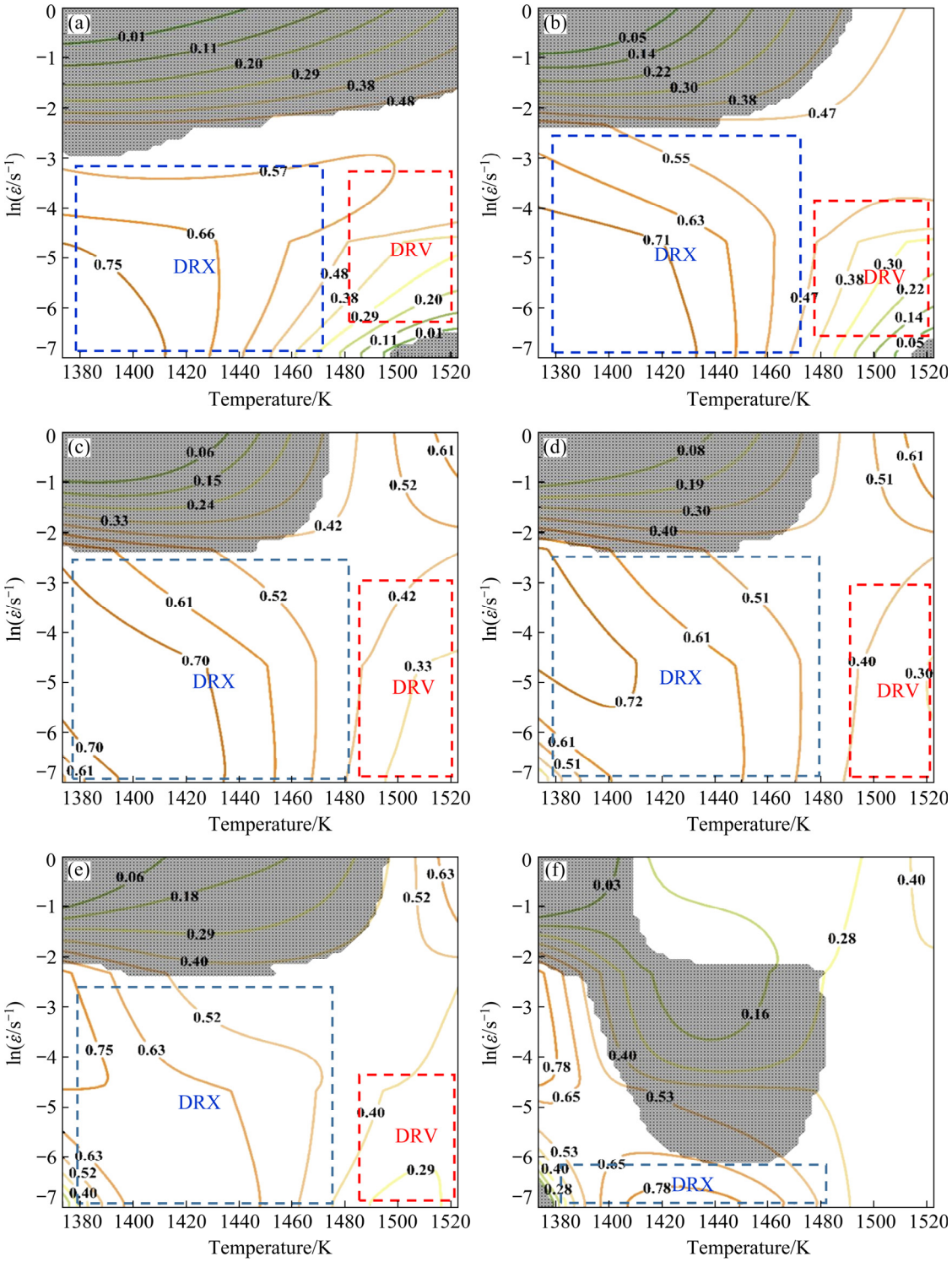

Fig. 16 Processing maps by Murty instability criterion with various strains: (a) ε=0.2; (b) ε=0.3; (c) ε=0.4; (d) ε=0.5; (e) ε=0.6; (f) ε=0.7

4 Conclusions

(1) The value of apparent deformation activation energy (Q) of the in-situ TiAl matrix composites with borides precipitation is calculated to be 691.51 kJ/mol. The novel constitutive equation is established as $\dot{\varepsilon}=3.8\times10^{23}\cdot[\sinh(0.00466\sigma)]^{3.05}\exp[-695506/(8.314T)]$. The processing maps by Murty instability criterion indicate the stable processing region in conditions of 1100−1200 °C, 0.001−0.1 s^{-1} and 1200−1250 °C,

0.001−0.1 s^{-1}.

(2) In the temperature range of 1100−1200 °C, the nucleation and growth of recrystallized γ and α_2 grains dominate the deformation of in-situ TiAl matrix composites below or above $T_{\alpha\rightarrow\alpha_2}$ at low strain rates (<0.1 s^{-1}). Meanwhile, the TiB obstacles can cause dislocation pile-ups to promote the nucleation of recrystallized grains. Additionally, boron addition can increase the fraction of α phase and decrease the transformation temperatures of $\gamma\rightarrow\alpha$ and $\alpha_2\rightarrow\alpha$, which dramatically enhances the fraction of recrystallized α_2 grains above $T_{\alpha\rightarrow\alpha_2}$.

(3) With the temperature increasing to 1250 °C, the dynamic recovery of disordered α phase dominates the deformation of in-situ TiAl matrix composites at low strain rates (<0.1 s^{-1}). Based on the grain refinement and the increased fraction of α phase, the dynamic recovery of disordered α phase caused by sub-grains formation, grain boundary bulging and dislocation gliding is promoted at 1250 °C.

Acknowledgments

This study was supported by the National Natural Science Foundation of China (No. 52101034), the Scientific and Technological Research Program of Chongqing Municipal Education Commission, China (No. KJQN202101138) and the Scientific Research Foundation of Chongqing University of Technology, China (No. 2020ZDZ003).

References

[1] SHEN Jing-yuan, HU Lian-xi, ZHANG Ling-yu, LIU Wen-chao, FANG Ai-wei, SUN Yu. Synthesis of TiAl/Nb composites with concurrently enhanced strength and plasticity by powder metallurgy [J]. Materials Science and Engineering A, 2020, 795: 139997.

[2] YANG Xin, XI Zheng-ping, LIU Yong, TANG Hui-ping, HU Ke, JIA Wen-peng. Microstructure and fracture toughness of a TiAl−Nb composite consolidated by spark plasma sintering [J]. Transactions of Nonferrous Metals Society of China, 2012, 22: 2628−2632.

[3] HU Yuan-tao, ZHENG Lei, YAN Hao-jie, WU Lian-kui, LIN Xiang-jun, CAO Fa-he, JIANG Mei-yan. Improving hot corrosion resistance of aluminized TiAl alloy by anodization and pre-oxidation [J]. Transactions of Nonferrous Metals Society of China, 2021, 31: 193−206.

[4] WANG Da-qun, SUN Dong-li, HAN Xiu-li, WANG Qing. In situ Ti_2AlN reinforced TiAl-based composite with a novel network structure: Microstructure and flexural property at elevated temperatures [J]. Materials Science and Engineering A, 2019, 742: 231−240.

[5] LI A B, CUI X P, WANG G S, QU W, LI F, ZHANG X X, GAN W C, GENG L, MENG S H. Fabrication of in situ Ti_5Si_3/TiAl composites with controlled quasi-network architecture using reactive infiltration [J]. Materials Letters, 2016, 185: 351−354.

[6] LI Ming-ao, XIAO Shu-long, CHEN Yu-yong, XU Li-juan, TIAN Jing. The effect of boron addition on the high-temperature properties and microstructure evolution of high Nb containing TiAl alloys [J]. Materials Science and Engineering A, 2018, 733: 190−198.

[7] REN Li-rong, QIN Shui-jie, ZHAO Si-hao, XIAO Hua-qiang. Fabrication and mechanical properties of Ti_2AlC/TiAl composites with co-continuous network structure [J]. Transactions of Nonferrous Metals Society of China, 2021, 31: 2005−2012.

[8] WANG W D, MA Y C, CHEN B, GAO M, LIU K, LI Y Y. Effects of boron addition on grain refinement in TiAl-based alloys [J]. Journal of Materials Science & Technology, 2010, 26: 639−647.

[9] KARTAVYKH A V, GORSHENKOV M V, TCHERDYNTSEV V V, PODGORNY D A. On the state of boride precipitates in grain refined TiAl-based alloys with high Nb content [J]. Journal of Alloys and Compounds, 2014, 586: S153−S158.

[10] HU Da-wei. Role of boron in TiAl alloy development: A review [J]. Rare Metals, 2016, 35: 1−14.

[11] CHEN C L, LU W, LIN J P, HE L L, CHEN G L, YE H Q. Orientation relationship between TiB precipitate and γ-TiAl phase [J]. Scripta Materialia, 2007, 56: 441−444.

[12] LIU B G, LIU L H, XING W D, LIU R C, YANG R, WITHEY P A, ZHU J, YU R. Structural stability and the alloying effect of TiB polymorphs in TiAl alloys [J]. Intermetallics, 2017, 90: 97−102.

[13] LI Jing, JEFFS S, WHITTAKER M, MARTIN N. Boride formation behaviour and their effect on tensile ductility in cast TiAl-based alloys [J]. Materials & Design, 2020, 195: 109064.

[14] HU D. Effect of boron addition on tensile ductility in lamellar TiAl alloys [J]. Intermetallics, 2002, 10: 851−858.

[15] LI Ming-ao, XIAO Shu-long, CHEN Yu-yong, XU Li-juan, TIAN Jing. The effect of boron addition on the deformation behavior and microstructure of β-solidify TiAl alloys [J]. Materials Characterization, 2018, 145: 312−322.

[16] LI Ming-ao, XIAO Shu-long, XU Li-juan, CHEN Yu-yong, TIAN Jing, ZHANG Bao-you. Mechanical properties, deformation behavior and microstructure evolution of Ti−43Al−6Nb−1Mo−1Cr alloys [J]. Materials Characterization, 2018, 136: 69−83.

[17] GRAEF M D, HARDWICK D A, MARTIN P L. Structural evolution of titanium di-borides in wrought Ti−47at.%Al−2Mo−0.2B [C]//DAROLIA R, LEWANDOWSKI J, LIU C T, MARTIN P L, MIRACLE D, NATHAL M V. Structural intermetallics. PA, Warrendale: TMS, 1997, 185.

[18] LI Jian-bo, LIU Yong, WANG Yan, LIU Bin, HE Yue-hui. Dynamic recrystallization behavior of an as-cast TiAl alloy during hot compression [J]. Materials Characterization, 2014, 97: 169−177.

[19] SCHWAIGHOFER E, CLEMENS H, LINDEMANN J, STARKD A, MAYER S. Hot-working behavior of an advanced intermetallic multi-phase γ-TiAl based alloy [J], Materials Science and Engineering A, 2014, 614: 297−310.

[20] ZONG Ying-ying, WEN Dao-sheng, LIU Zu-yan, SHAN De-bin. γ-phase transformation, dynamic recrystallization and texture of a forged TiAl-based alloy based on plane strain compression at elevated temperature [J]. Materials & Design, 2016, 91: 321–330.

[21] WU B L, WAN G, ZHANG Y D, DU X H, WAGNER F, ESLING C. Fragmentation of large grains in AZ31 magnesium alloy during ECAE via route A [J], Materials Science and Engineering A, 2010, 527: 3365–3372.

[22] YE Pei-hao, JIN Xu-chen, FANG Wen-bin, LI Xue-wen, WU Hao, FAN Guo-hua. Hot deformation behavior and microstructure evolution of a high Nb containing PM TiAl composite reinforced with Ti_2AlC particles [J]. Materials Today Communications, 2021, 29: 102862.

[23] LI Ming-ao, LI Juan, ZHOU Tao, XIAO Shu-long, CHEN Yu-yong, XU Li-juan, HU Li, SHI Lai-xin. The investigation of microstructure evolution, deformation behavior and processing performance of the high niobium containing TiAl alloys [J]. Intermetallics, 2021, 138: 107336.

[24] WU Xin-hua. Review of alloy and process development of TiAl alloys [J]. Intermetallics, 2006, 14: 1114−1122.

[25] KAINUMA R, FUJITA Y, MITSUI H, OHNUMA I, ISHIDA K. Phase equilibria among α (hcp), β (bcc) and γ ($L1_0$) phases in Ti−Al base ternary alloys [J]. Intermetallics, 2000, 8: 855−867.

[26] DING J J, QIN Q W, HAO S M, WANG X T, CHEN G L. Partial phase diagram of the Ti−Al binary system [J]. Journal of Phase Equilibria, 1996, 17: 117−120.

[27] MIRZADEH H, CABRERA J M, NAJAFIZADEH A. Modeling and prediction of hot deformation flow curves [J]. Metallurgical and Materials Transactions A, 2012, 43: 108−123.

[28] TIAN Su-gui, LV Xiao-xia, YU Hui-chen, WANG Qi, JIAO Ze-hui, SUN Hao-fang. Creep behavior and deformation feature of TiAl−Nb alloy with various states at high temperature [J]. Materials Science and Engineering A, 2016, 651: 490−498.

[29] SCHWAIGHOFER E, SCHLOFFER M, SCHMOELZER T, MAYER S, LINDEMANN J, GUETHER V, KLOSE J, CLEMENS H. Influence of heat treatments on the microstructure of a multi-phase titanium aluminide alloy [J]. Practical Metallography, 2012, 49: 124−137.

[30] SCHWAIGHOFER E, CLEMENS H, MAYER S, LINDEMANN J, KLOSE J, SMARSLY W, GÜTHER V. Microstructural design and mechanical properties of a cast and heat treated intermetallic multi-phase γ-TiAl based alloy [J]. Intermetallics, 2014, 44: 128−140.

[31] SCHWAIGHOFER E, RASHKOVA B, CLEMENS H, STARK A, MAYER S. Effect of carbon addition on solidification behavior, phase evolution and creep properties of an intermetallic β-stabilized γ-TiAl based alloy [J]. Intermetallics, 2014, 46: 173−184.

[32] QIANG Feng-ming, BOUZY E, KOU Hong-chao, ZHANG Yu-dong, WANG Ling-ling, LI Jin-shan. Grain fragmentation associated continuous dynamic recrystallization (CDRX) of hexagonal structure during uniaxial isothermal compression: High-temperature α phase in TiAl alloys [J]. Intermetallics, 2021, 129: 107028.

[33] MCQUEEN H J, RYAN N D. Constitutive analysis in hot working [J]. Materials Science and Engineering A, 2002, 322: 43−63.

[34] JIANG Hai-tao, ZENG Shang-wu, ZHAO Ai-min, DING Xiao-nan, DONG Peng. Hot deformation behavior of β phase containing γ-TiAl alloy [J]. Materials Science and Engineering A, 2016, 661: 160–167.

[35] TIAN Shi-wei, JIANG Hai-tao, GUO Wen-qi, ZHANG Gui-hua, ZENG Shang-wu. Hot deformation and dynamic recrystallization behavior of TiAl-based alloy [J]. Intermetallics, 2019, 112: 106521.

[36] LIN Y C, XIA Y C, CHEN X M, CHEN M S. Constitutive descriptions for hot compressed 2124-T851 aluminum alloy over a wide range of temperature and strain rate [J]. Computational Materials Science, 2010, 50: 227−233.

[37] WANG Yong-jian, PENG Jian, ZHONG Li-ping, PAN Fu-sheng. Modeling and application of constitutive model considering the compensation of strain during hot deformation [J]. Journal of Alloys and Compounds, 2016, 681: 455−470.

[38] NARAYANA MURTY S V S, NAGESWARA RAO B. On the development of instability criteria during hot working with reference to IN 718 [J]. Materials Science and Engineering A, 1998, 254: 76−82.

[39] RAVICHANDRAN N, PRASAD Y V R K. Dynamic recrystallization during hot deformation of aluminum: A study using processing maps [J]. Metallurgical Transactions A, 1991, 22: 2339−2348.

[40] RADHAKRISHNA BHAT B V, MAHAJAN Y R, ROSHAN H M, PRASAD Y V R K. Processing map for hot working of powder [J]. Metallurgical Transactions A, 1992, 23: 2223−2230.

[41] XU Wen-chen, JIN Xue-ze, SHAN De-bin, CHAI Bai-xin. Study on the effect of solution treatment on hot deformation behavior and workability of Mg−7Gd−5Y−0.6Zn−0.8Zr magnesium alloy [J]. Journal of Alloys and Compounds, 2017, 720: 309−323.

[42] NARAYANA MURTY S V S, NAGESWARA RAO B. Instability map for hot working of 6061 Al−10vol% metal matrix composite [J]. Journal of Physics D: Applied Physics, 1998, 31: 3306–3311.

[43] PRASAD Y V R K, SESHACHARYULU T. Processing maps for hot working of titanium alloys [J]. Materials Science and Engineering A, 1998, 243: 82–88.

硼化物原位自生增强 TiAl 基复合材料的组织演化、热变形行为及加工工艺设计

李明骜[1,2,3]，李 娟[1]，周 涛[1]，胡 励[1]，时来鑫[1]，陈玉勇[2,3]，徐丽娟[3]，肖树龙[2,3]

1. 重庆理工大学 材料科学与工程学院，重庆 400054；
2. 哈尔滨工业大学 金属精密热加工国家级重点实验室，哈尔滨 150001；
3. 哈尔滨工业大学 材料科学与工程学院，哈尔滨 150001

摘 要：硼元素添加造成的相转变和硼化物析出等因素会对原位 TiAl 基复合材料显微组织演化及热变形行为产生影响。利用等温压缩实验、扫描电子显微技术以及透射电子显微技术等研究材料的动态再结晶和动态回复机制，并计算出其表现变形激活能为 691.506 kJ/mol。在 1100~1200 ℃温度区间，再结晶 γ 和 α 晶粒的形核长大分别主导 $\alpha_2 \rightarrow \alpha$ 相转变温度上、下的热变形行为。α 相的动态回复主导材料在 1250 ℃低应变速率下的热变形行为；同时，硼元素会提高 α 相含量，降低 $\gamma \rightarrow \alpha$ 和 $\alpha_2 \rightarrow \alpha$ 相转变温度，进而促进加载过程中回复 α 相晶粒的形核长大。根据新建的本构模型，对 TiAl 基复合材料的变形机制和加工工艺进行详细阐述.

关键词：原位 TiAl 基复合材料；硼化物；变形机制；显微组织演化；动态再结晶；动态回复

(Edited by Bing YANG)